A global eddying hindcast ocean simulation with OFES2

Hideharu Sasaki[1], Shinichiro Kida[2,1], Ryo Furue[1], Hidenori Aiki[3,1], Nobumasa Komori[1], Yukio Masumoto[4,1], Toru Miyama[1], Masami Nonaka[1], Yoshikazu Sasai[5], Bunmei Taguchi[6,1]

[1]Application Laboratory, Japan Agency for Marine-Earth Science and Technology, Yokohama, Japan
[2]Research Institute for Applied Mechanics, Kyushu University, Kasuga, Japan
[3]Institute for Space-Earth Environmental Research, Nagoya University, Nagoya, Japan
[4]Graduate School of Science, The University of Tokyo, Tokyo, Japan
[5]Research Institute for Global Change, Japan Agency for Marine-Earth Science and Technology, Yokosuka, Japan
[6]Faculty of Sustainable Design, University of Toyama, Toyama, Japan

Correspondence to: Hideharu Sasaki (sasaki@jamstec.co.jp)

Abstract. A quasi-global eddying ocean hindcast simulation using a new version of our model called "OFES2" (Ocean General Circulation Model for the Earth Simulator version 2) was conducted to overcome several issues with unrealistic properties in its previous version "OFES". This paper describes the model and the simulated oceanic fields in OFES2 compared with OFES and also observed data. A sea-ice model and a tidal mixing scheme were implemented in OFES2, which was forced by a newly created surface atmospheric dataset called JRA55-do and simulated the oceanic fields from 1958 to 2016. We found several improvements in OFES2 over OFES: smaller biases in the global sea surface temperature and sea surface salinity and the water properties in the Indonesian and Arabian Seas. The time series of the Niño3.4 and Indian Ocean Dipole (IOD) indexes are somewhat better in OFES2 than in OFES. Unlike the previous version, OFES2 reproduces more realistic anomalous low sea surface temperatures during a positive IOD event. One possible cause for these improvements in El Niño and IOD events is the replacement of the atmospheric dataset. On the other hand, several issues remained unrealistic, such as the pathways of the Kuroshio and Gulf Stream and the unrealistic spreading of salty Mediterranean overflow. Given the worldwide use of the previous version and the improvements presented here on it, the output from OFES2 will be useful in studying various oceanic phenomena with broad spatiotemporal scales.

1 Introduction

The global ocean includes phenomena with various spatial scales. Basin-scale circulations occur over thousands of kilometers, while oceanic fronts, western boundary currents, and the Antarctic Circumpolar Current (ACC) have widths of approximately or less than 100 km. Mesoscale eddies, ubiquitous around these currents and in the ocean interior, have a spatial scale of a few tens of kilometers in the sub-Arctic ocean to a few hundred kilometers in the subtropics (Chelton et al., 1998). The location and strength of oceanic fronts, currents, and mesoscale eddies also change over time (e.g., Sasaki and Schneider, 2011; Qiu and Chen, 2010; Zhai et al., 2008).

Observations are crucial for understanding the ocean, but their data coverage and resolution are limited. Since the 2000s, gridded hydrographic products based on Argo float observations (e.g., Roemmich et al., 2009, Hosoda et al., 2008) have been able to capture global ocean properties at a resolution of approximately 300 km. However, such a spatial resolution is not adequate to observe currents, mesoscale eddies, and frontal structures. Satellite observations can provide high-resolution data of the sea surface height (SSH) and temperature (SST), etc. but are limited to surface measurements. Global eddying simulations, therefore, have become a useful and convenient tool for understanding the ocean. Computational power has increased exponentially, and over past decades, several research groups have been conducting global eddying ocean simulations at horizontal resolutions of approximately 10 km using the Parallel Ocean Program (POP, Maltrud and McClean, 2005), the Hybrid Coordinate Ocean Model (HYCOM, Chassignet et al., 2006), the Max Planck Institute ocean model (MPIOM, Jungclaus et al., 2013), and the Ocean General Circulation Model (OGCM) for the Earth Simulator (OFES, Masumoto et al., 2004). The realistic long-term hindcast global eddying ocean simulation outputs from OFES have been widely used in the community (http://www.jamstec.go.jp/res/ress/sasaki/ofes_publication.html).

The outputs from global eddying ocean simulations have provided unprecedented information about oceanic phenomena on wide spatiotemporal scales in areas where observational data are limited. These simulations create a significant amount of data, which are very informative because the data exhibit oceanic phenomena from around the globe with the scales from mesoscales to large scales and their variations from intraseasonal to decadal timescales. Sharing simulation outputs among the community is crucial, and such use of OFES (Sasaki et al., 2008) has led to research achievements in various topics (see details in Masumoto 2010), such as in oceanic phenomena from intraseasonal (e.g., Hu et al. 2018) to decadal variations (e.g., Taguchi et al. 2017) and mesoscale eddies (e.g., Aoki et al. 2016). However, numerical models are not perfect. Model deficiencies and biases exist, and the usage of simulation outputs in the community has led to findings of where these limitations exist and their possible causes. One of the major problems of OFES seems to be its surface wind stress fields. Kutsuwada et al. (2019) showed that the thermocline depth in the subtropical northwestern Pacific was too shallow due to unrealistic wind stress. The second problem is the lack of tidally induced vertical mixing. Masumoto et al. (2008) found unrealistic water properties within the Indonesian seas, where tidally induced vertical mixing is considered significant (Ffield and Gordon, 1996). The third problem is the lack of sea ice. Therefore, the sea surface salinity in OFES was strongly restored to monthly climatological observations.

This paper highlights how an updated OFES improved the hindcast simulation outputs from OFES. This model was forced by surface forcing based on 3-hourly atmospheric reanalysis data at a finer horizontal resolution. A tidal mixing scheme and a sea-ice model were added, and we call the standard hindcast simulation using this new version OFES2 (Fig. 1). Section 2 describes OFES2, and Section 3 examines its simulated mean oceanic fields. Section 4 examines the time variability based on climate indexes of El Niño and the Indian Ocean Dipole Mode (IOD). We will further examine the IOD events and highlight the simulated SST distribution around the eastern pole of the IOD. A summary and discussion are provided in Section 5.

2 Descriptions of OFES2 compared with OFES

OFES2 is an update of a quasi-global eddying hindcast simulation: OFES (Sasaki et al., 2008). It is based on Modular Ocean Model (MOM) version 3 (Pacanowski and Griffies, 1999) and utilizes the latitude and longitude grid system. The horizontal resolution of 0.1° remains the same as that in OFES, but the model setup and parameterization are added to reduce the model biases that exist in OFES. The model configuration of OFES2 will be described first, and the differences from OFES will be described next.

The domain extends from 76° S to 76° N without polar regions. The horizontal resolution is 0.1°, and the number of vertical levels is 105 with a maximum depth of 7,500 m. The thickness of each layer within the upper 100 m is 5 m. The thickness gradually increases and 55 levels exist within the upper 500 m. We constructed the bottom topography with partial bottom cells (Adcroft et al., 1997) using the bathymetry dataset ETOPO1 (Amante and Eakins, 2009). Although the model domain does not include the polar region, a sea-ice model (Komori et al., 2005) was internally implemented into OFES2 to simulate the Antarctic Sea and the Subarctic seas, including the Sea of Okhotsk, more realistically. The sea-ice model employs two-category, zero-layer thermodynamics (Hibler 1979) and elastic-viscous-plastic rheology (Hunke and Dukowicz, 2002).

A biharmonic operator is used for horizontal mixing to suppress computational noise with a viscosity of -27×10^9 m^4 s^{-1} and a diffusivity of -9×10^9 m^4 s^{-1}. The drag coefficient is 2.5×10^{-3} (non-dimensional) for linear bottom drag. For vertical mixing, we added diffusivities from the tidal mixing scheme developed by Jayne and St. Laurent (2001) and St. Laurent et al. (2002) to those estimated from the mixed layer vertical mixing scheme of a statistical closure model (Noh and Kim, 1999). In the tidal mixing scheme, the three-dimensional diffusivities are estimated from the energy flux at the ocean bottom and the local buoyancy frequency with the parameters of dissipation efficiency, mixing efficiency, and vertical scale. These parameters are the same as those used by St. Laurent et al. (2002). We used a constant barotropic tidal current of K1 and M2 as the largest diurnal and semidiurnal tidal components in the FES2012 finite-element tide model (Carrère et al., 2012) and the bottom topographic slopes instead of roughness to estimate the energy flux at the ocean bottom (Tanaka et al., 2007). The simulated vertical diffusivities are large over rough bottom topographies and in areas with large tidal motions (Fig. 2a). The diffusivities exponentially decay in an upward direction (e.g., along 10°N in Fig. 2b). These are similar to the simulated diffusivities of Figs. 1 and 2 in the study by St. Laurent et al. (2002). The diffusivities do not change much over time because the tidal flow used to estimate the energy flux is assumed to be constant, and therefore, the diffusivities change in time only through changes in the local stratification.

We used the 3-hourly atmospheric surface dataset JRA55-do ver.08 (Tsujino et al., 2018) to estimate surface fluxes in OFES2. This dataset is based on the JRA55 atmospheric reanalysis at a horizontal resolution of approximately 55 km (Kobayashi et al., 2015). Momentum and heat fluxes are calculated with the bulk formulas proposed by Large and Yeager (2004). Note that we used the relative wind speed considering the surface current to estimate the surface momentum flux. We also included the effects of river runoff at river mouths as additional freshwater flux using a monthly mean

climatological river runoff dataset from Coordinated Ocean-Ice Reference Experiments (CORE) version 2 (Large and Yeager, 2004). The sea surface salinity (SSS) is restored to monthly climatological values of the WOA13 v2 observations (Zweng et al., 2013) with a 15-day timescale to avoid unrealistic salinity fields.

Since the polar regions are not simulated, the temperature and salinity are restored at all depths to the monthly climatological values from the same WOA13 v2 observations (Locarnini et al., 2013; Zweng et al., 2013) within a distance of 3° from the northern and southern boundaries of the model domain. The restoring time-scale linearly increases from 1 day at the boundary to infinity at the inner end of the restoring band. Additionally, the temperature and salinity near the straits of Gibraltar, Hormuz, and Bab el-Mandeb are restored to observations at all depths since the horizontal resolution of the model is inadequate to capture dynamics within these straits (Fig. 3). The strait of Gibraltar is where the Atlantic Ocean connects to the Mediterranean Sea and the straits of Hormuz and Bab el-Mandeb are where the Persian Gulf and the Red Sea are connected to the Indian Ocean, respectively.

OFES (Sasaki et al., 2008), which follows a 50-year climatological simulation, has been integrated from 1950 to the present (Masumoto et al., 2004). OFES2 was integrated from 1958 to 2016 and started with the temperature and salinity fields of OFES from January 1, 1958. Table 1 is the list of the updates for OFES2 compared to OFES. The maximum depth of OFES2 is increased to 7,500 m from 6,065 m. The surface fluxes are now based on 3-hourly data rather than daily data to capture the diurnal cycle. Momentum fluxes are based on a bulk formula using the relative wind speed rather than that estimated in the reanalysis. The distribution of momentum flux curl in OFES2 differs much compared with that in OFES (Fig. S1). The mixed layer mixing scheme is updated by replacing the KPP scheme based on an empirical approach (Large et al., 1994) by a statistical closure model (Noh and Kim, 1999). A tidal mixing scheme and a sea-ice model are newly included. River runoff is also added as additional freshwater flux. SSS is restored with a 15-day time scale rather than a 6-day timescale: a 150-day time scale and a 60-day time scale with respect to 50 m depth respectively. The timescale was relaxed compared to OFES, where neither sea ice nor river runoff was used.

3 Mean oceanic fields

We next discuss improvements in the mean oceanic fields in OFES2 from OFES by comparing those to the observations. The mean temperature and salinity fields at a horizontal resolution of 0.25° averaged over 2005-2012 from the World Ocean Atlas 2013 version 2 (WOA13, Locarnini et al., 2013, Zweng et al., 2013) are used, which include a large number of Argo float observations. During this period, both OFES2 and OFES were well spun up. Satellite-observed SSH over 1993-2016 from AVISO is used to examine the simulated oceanic circulations and SSH variations in both OFES2 and OFES. To see how the sea-ice model works in OFES2, the climatological data of sea-ice cover averaged over 2005-2012 from HadISST version 1 (Rayner et al., 2003) is compared with the data in OFES2.

3.1 Global oceanic fields

3.1.1 Sea surface temperature and salinity

130   Figures 4a and 4c show the 8-year mean SST and SSS biases averaged over 2005-2012 in OFES2 against WOA13. For SST (Fig. 4a), the bias is less than 1°C in most parts of the globe. A weak cold bias broadly spreads over the subtropical Pacific and Indian Oceans and the Arctic Ocean and weak warm bias spreads over the sub-Arctic Pacific, the sub-Arctic Atlantic, and the Southern Oceans. However, we found prominent biases in several regions. Warm biases (> 1 °C) appear in the South Pacific (170°-130° W and 55° S) and to the north of the Kuroshio Extension (140°-170° E and 35°-40° N). In the North

135   Atlantic, along the Gulf Stream and the North Atlantic Current and in the Labrador and Norwegian Seas, several large warm and cold biases (magnitudes larger than 1°C) are present. One possible cause of these biases is the unrealistic current pathway of the Gulf Stream. The Gulf Stream does not turn to the north at approximately 40° N, which we will examine more in detail in the next section.

The mean SSS biases in OFES2 (Fig. 4c) are smaller than 0.2 psu in most regions. This feature is partly due to the

140   restoring boundary condition, but several large biases (larger than 0.2 psu) exist sporadically. The salty bias (> 0.4 psu) in the North Atlantic (30° W and 50° N) likely comes from the unrealistic Gulf Stream pathway, similar to the SST bias mentioned above. The salty bias (> 0.4 psu) also appears to the north of South America and in the northern part of the Bay of Bengal, which surrounds the fresh bias respectively. One reason of the large salty bias is probably due to the underestimation of freshwater from the Amazon and Ganges-Brahmaputra Rivers, respectively. The impacts of physical processes near the

145   river mouth such as horizontal and vertical mixing, coastal circulation, and tidal mixing should be included to improve the bias. In addition, there are large salty and fresh biase in the Chukchi Sea and large salty biases in the Nordic and Labrador Seas and along the coast of Greenland. These SSS biases are possibly attributed to unrealistic sea-ice distribution in the Chukchi Sea (Fig. 9g) and unrealistic circulations due to the northern boundary of OFES2.

Figures 4b and 4d show the 8-year mean SST and SSS biases averaged over 2005-2012 in OFES against WOA13. The

150   SST biases are much smaller in OFES2 (Fig. 4a) than in OFES (Fig. 4b). Cold (warm) SST biases with large amplitudes appear in the equatorial and subtropical regions (high-latitude regions) in both hemispheres in OFES (Fig. 4b). The centers of the cold biases (< -1°C) zonally spread along 15° N and 15° S in the Pacific Ocean and the northwestern and southeastern Indian Ocean. Patches of warm biases (> 1°C) exist in the Antarctic Ocean to the south of the Antarctic Circumpolar Current (ACC). Prominent warm biases (> 1°C) appear in the northwestern Pacific, the Sea of Okhotsk, and along the west coasts of

155   South America and Southern Africa. The prominent warm biases along the west coasts in OFES are presumably associated with unrealistic coastal currents and upwelling, which are driven by unrealistic wind stresses near the coasts in the NCEP reanalysis (Fig. S1). These reductions in OFES2 are likely a result of using the bulk formula (Large and Yeager, 2004) and the atmospheric surface data (JRA55-do), which are optimized to drive OGCMs (Tsujino et al., 2018). Additionally, the implementation of a sea-ice model in OFES2 may contribute to the decreases in the warm biases in the Arctic Ocean and the

160   Sea of Okhotsk.

The mean SSS biases in OFES2 (Fig. 4c) are also much reduced compared to those in OFES (Fig. 4d), especially in the tropical and subtropical regions. These bias reductions are also likely due to the bulk formula and atmospheric data used in OFES2. We notice that the global distribution of the biases in OFES (Fig. 4d), prominent in the Arctic Ocean is quite similar to the difference between WOA98 (Conkright et al., 1998) and WOA13 averaged over 2005-2012 (Fig. 4f). This similarity suggests that the SSS fields in OFES are too much restored to WOA98. In contrast, the global distribution of the SSS biases in OFES2 (Fig. 4c) does not resemble the difference between long-term mean WOA13 and WOA13 over 2005-2012 (Fig. 4e). The weak restoring in OFES2 does not greatly constrain the simulated SSS. Therefore, the SSS bias in OFES2 (Fig. 4c) comes from something other than the restoring such as the unrealistic path ways of Kuroshio and Gulf Stream and the unrealistic sea-ice distribution in the Chukchi Sea as mentioned above.

3.1.2 Sea surface height and its variability

Figure 5 shows the average and standard deviation of the sea surface height (SSH) over 1993-2016 in OFES2, OFES, and AVISO. The large-scale distribution of the mean SSHs in OFES2 (Fig. 5a) agrees well with that in AVISO (Fig. 5c), suggesting that OFES2 reproduces the global ocean circulations. The SSH variability (Fig. 5d) is large around the Gulf Stream, the Kuroshio, and the ACC, which also resembles that in AVISO (Fig. 5f). This large variability is mostly due to high activities of mesoscale eddies and shifts in frontal positions (e.g., Chelton et al., 2007).

However, there are regional differences in the mean SSH distribution and its standard deviation in OFES2 compared to those in AVISO. The mean SSH contours along the Gulf Stream extend towards the northeast (Fig. 5a), while a sharp northern turn is observed at approximately 40° W (Fig. 5c). The SSH variability is large along this simulated Gulf Stream (Fig. 5d). The zonal extension of the mean SSH contours along the Azores Current at approximately 33° N in the northeastern Atlantic (Fig. 5c) and large SSH variability accompanied by this current (Fig. 5f) are recognizable in AVISO but do not appear in OFES2 (Fig. 5a and Fig. 5d). For the Kuroshio in OFES2, the SSH variability is too large along the southern coast of Japan. This large variability is due to the unrealistic detachment of the Kuroshio from Kyushu. Around subtropical countercurrents in the North Pacific and the South Indian Ocean and in most regions away from the strong currents, the SSH variability is slightly smaller in OFES2 than in AVISO. We discuss these issues in Section 5.

Compared to OFES (Fig. 5b), the mean SSH in OFES2 (Fig. 5a) shows improvements. In the northern and southern subtropical gyres of the Pacific, the SSH contours are oriented more in the north-south direction in OFES (Fig. 5b) than in OFES2 and AVISO (Figs. 5a and 5c). In contrast, the subtropical gyres of the Atlantic and Indian Oceans do not have this difference. One possible cause for this improvement in the SSH field in OFES2 is the replacement of atmospheric wind driving OFES2 by JRA55-do. The SSH variability around strong currents such as the Gulf Stream, the Kuroshio, and the ACC (Fig. 5d) in OFES2 is comparable to AVISO observations (Fig. 5f), which is reduced somewhat compared to OFES (Fig. 5e). The northwestward extent with SSH variability to the west of South Africa that corresponds to propagations of Agulhas Rings is improved in OFES2, which is too distinct in OFES due to unrealistic long-lived rings. These SSH

variability reductions in OFES2 are possibly due to eddy killing effect in the estimation of surface momentum flux using the relative wind (e.g. Renault et al. 2017, 2019a).

3.2 Impact of tidal mixing on water mass property

Tidal mixing is considered to mix the ocean, especially above rough-bottom topography. Previous studies have suggested that the Indonesian seas are regions where such mixing significantly impacts the water mass properties (e.g., Ffield and Gordon, 1996). Koch-Larrouy et al. (2007) demonstrated how inclusion of the local tidal mixing scheme can improve the subsurface water mass in the Indonesian seas and the eastern Indian Ocean. As mentioned in the introduction, unrealistic water mass properties in the subsurface of Indonesian Seas were one of the major biases recognized in OFES (Masumoto et al., 2008), which motivated us to add the tidal mixing scheme in OFES2.

A comparison of subsurface salinity biases in the Indonesian seas shows significant improvement in OFES2 (Figs. 6a and 6d) from OFES (Figs. 6b and 6e). The saltier bias at a depth of 135 m is large (> 0.5 psu) in the northern Banda Sea in OFES but is greatly reduced in OFES2. To the south of the Sunda Islands, the saltier biases are prominent both at depths of 135 m (> 0.2 psu) and 325 m (> 0.5 psu) in OFES but are greatly reduced in OFES2. The remaining salty biases in OFES2 may be partially due to lack of nonlocal tidal mixing (e.g. Nagai et al., 2017), as discussed in Sasaki et al. (2018). This result supports the importance of tidal mixing on the water mass transformation in the Indonesian seas.

The Kuril Strait between the North Pacific and the Sea of Okhotsk is another location where previous studies (e.g., Nakamura et al., 2006) suggested the importance of tidal mixing on the water mass properties of the North Pacific Intermediate Water (NPIW). The vertical section of salinity along 165° E in WOA13 shows that this subsurface low-salinity water is accompanied by the NPIW, which both OFES2 and OFES demonstrate well (Fig. S2) although this water mass distribution is improved a little more in OFES2 than OFES. The result suggests that the tidal mixing scheme in OFES2 does not affect the water properties much, which supports the results using an eddy-permitting model by Tanaka et al. (2010). Nakamura et al. (2006) may have added too large vertical diffusivity (0.02 $m^2 s^{-1}$) in the strait at all depths in their OGCM, which probably led to too strong impacts on the water properties.

3.3 Salty outflows from marginal seas

OFES could not accurately simulate high-salinity outflows from the Mediterranean Sea, the Persian Gulf, and the Red Sea to the open ocean. To represent the impact of these outflows in OFES2, we restored temperature and salinity near the straits. Proper representations of these outflows are considered important for simulating not only the subsurface but also the surface properties (e.g., Jia et al., 2000; Prasad et al. 2001; Sofianos and Johns, 2002).

Vertical sections of salinity averaged over 2005-2012 (Fig. 7) exhibit the salty outflows at the subsurface in the Arabian Sea and the Atlantic Ocean. For the Arabian Sea, the basic influence of the outflow appears to be captured in OFES2. The longitudinal section of mean salinity crossing the mouth of the Red Sea shows that OFES2 (Fig. 7a) mostly reproduces the eastward extent of salty water (> 35.5 psu) from 46° E at approximately 700 m depth, observed in WOA13 (Fig. 7c). This

225 feature corresponds to the salty outflow from the Red Sea. The eastward extension (> 35.5 psu), however, reaches too far at 70° E, and its depth of 700 m is too stable over the basin compared to that in WOA13. OFES2 (Fig. 7d) also generally demonstrates the southward spreading of salty outflow from the Persian Gulf: salty water (> 35.5 psu) spreads southward from 25° N above 1000 m in WOA13 (Fig. 6f). However, the high salinity core (> 35.5 psu) at a depth of 800 m is slightly too distinct and deep in OFES2 (Fig. 7d).

230 However, we found that OFES2 does not reproduce the salty outflow from the Mediterranean Sea into the Atlantic Ocean well by restoring temperature and salinity near the Strait of Gibraltar. A zonal vertical section of salinity along 36° N in the eastern Atlantic Ocean in WOA13 (Fig. 7i) exhibits the westward extension of salty water (> 35.8 psu) to 25° W at approximately 1100 m depth and a thick layer with almost constant salinity of 35.7 psu over 500-1100 m depths to the west of 26° W. However, the westward extent of high salinity is still weak in OFES2 (Fig. 7g). This high salinity (> 36.0 psu)

235 remains to the east of 9° W at depths over 1000-1500 m, where OFES2 restores salinity to the observation (Fig. 3). Why the salty water does not spread westward much in OFES2 is unclear, but this phenomenon is possibly be connected to the bias found in the mid-ocean surface circulation in the North Atlantic (Figs. 5a and 5c). Entrainment of surface water to the Mediterranean outflow near the Strait of Gibraltar is suggested as the mechanism driving the Azores Current (Jia et al. 2000; Kida et al., 2008) and turning northward of the Gulf Stream (Jia et al., 2000).

240 The implementation of restoring temperature and salinity conditions at the straits resulted in significant improvements in the Arabian Sea from OFES without the setup. OFES2 reproduces the salty outflow from the Red Sea well (Fig. 7a) but OFES does not: there is no salty water at the subsurface along 13° N in the Arabian Sea (Fig. 7b). OFES2 also greatly improved the salty outflow from the Persian Gulf (Fig. 7d) from OFES (Fig. 7e). The meridional section along 65° E shows that the salinity of subsurface salty outflow in OFES (Fig. 7e) is much fresher by 0.3-0.5 psu than that in WOA13 (Fig. 7f),

245 and its depth of 1000 m is deeper than that in WOA13 (800 m). For the Mediterranean outflow, the improvement in OFES2 from OFES is marginal. Both OFES2 (Fig. 7g) and OFES (Fig. 7h) cannot reproduce the westward extent of the salty outflow from the Strait of Gibraltar found in WOA13 (Fig. 7i).

3.4 Subsurface field in the subtropical North Pacific

The subsurface water properties are sensitive to the wind stress product used. Kutsuwada et al. (2019) showed that wind

250 stress products affect the simulated oceanic fields in an OGCM not only at the surface but also in the subsurface. In the subtropical Pacific along 10° N where the subsurface bias is large in OFES (Fig. 4 of Kutsuwada et al. 2019), they found that the use of QuikSCAT wind stress (Kutsuwada, 1998) in another version of OFES, called OFES QSCAT (Sasaki et al., 2006), improves the subsurface water properties compared to OFES using wind stress from NCEP reanalysis (Kalnay et al., 1996).

The vertical profile of the mean temperatures in the subtropical Western Pacific in OFES2 (red curve) mostly overlaps

255 with that in WOA13 (black curve) (Fig. 8a). The maximum difference occurs at 280 m and is less than 1 °C. This region is characterized by subsurface salinity maximum (e.g., Nakano et al., 2005). Its depth agrees between OFES2 and WOA13 (Fig. 8b), and its peak salinity value differs a bit by 0.2 psu.

We found that the temperature and salinity biases in OFES2 improved significantly from OFES. In the thermocline between 50 m and 350 m depths, the temperature is much lower in OFES (Fig. 8a, blue curve) than in WOA13 (black curve).
260 The maximum difference is approximately 6 °C at a depth of approximately 150 m. The depth of the salinity maximum is much shallower in OFES (approximately 100 m depth) than in WOA13 (approximately 140 m depth) (Fig. 8b). The maximum difference in salinity between OFES and WOA13 is large (~0.4 psu). These biases are very similar to those found by Kutsuwada et al. (2019) in their comparison between OFES QSCAT and OFES (their Fig. 5). As Kutsuwada et al. (2019) suggested, these large biases in OFES possibly come from the surface momentum flux. The wind stress curl from NCEP
265 driving OFES along 10° N (blue curve in Fig. 8c) is relatively strong and fluctuates considerably in the longitudinal direction, which results in the anomalously shallow thermocline via too large Ekman upwelling. The wind stress curl in OFES2 (red curve in Fig. 8c) estimated by using 10-m wind in JRA55-do is comparable in amplitudes and variations to the satellite observations (red curve in Fig. 3c of Kutsuwada et al., 2019). The similarity between wind stress curl in OFES2 and the satellite observations comes from modifications of 10-m wind in JRA55-do using the satellite observations (Tsujino et al.,
270 2018).

3.5 Sea-ice distribution in OFES2

We implemented a sea-ice model in OFES2, which is not present in OFES. The domain of OFES2 excludes a large, central part of the Arctic Sea and the southern-most parts of the Ross Sea and the Weddell Sea. Figure 9 shows the distribution of monthly climatological sea-ice cover in the polar regions averaged over 2005-2012 compared to the observations from
275 HadISST. The sea-ice cover around Antarctica in March is realistic in OFES2 (Fig. 9a). The simulated sea ice covers most areas of the Weddell Sea, as found in HadISST (Fig. 9b). A bit of sea ice remains along the most coastline of East Antarctica (right side of the figure) in HadISST. However, OFES2 misses the observed sea-ice cover near the coast from 90° E to 180° E. The sea-ice distribution in September expands greatly compared to March in HadISST (Fig. 9d), and OFES2 exhibits its distributions very well (Fig. 9c). Off the coast of Victoria Land between 180° E and 150° E (lower side of the figure) and
280 along the southern boundary of the model domain (76° S) in the Ross Sea (160° E-150° W), the sea-ice concentration in OFES2 is somewhat lower than in HadISST.

The observed sea ice in the Arctic region in March covers the Chukchi Sea and seeps into the Bering Sea through the Bering Strait (Fig. 9f). OFES2 reproduces the observations well (Fig. 9e). However, the simulated sea ice spreads too much southward into marginal seas: the Baltic Sea, the Gulf of Saint Lawrence, and the Sea of Okhotsk. In September, unrealistic
285 sea-ice cover spreads in the Chukchi Sea (Fig. 9g), which does not exist in HaISST (Fig. 9h). This defect is possibly due to the artificial northern boundary in OFES2, which blocks the sea ice outflow (Kwok et al. 2004) through the Fram Strait.

The observed sea ice in September in the Arctic region decreased much: relatively small extent of the sea ice in 2005-2012 (Fig. 9h) compared with that in 1980s (Fig. S3h). However, OFES2 fails to simulate the trend probably because of the limited domain, which does not cover most of the Arctic Sea. In the Antarctic region, the extent of sea ice appears not to
290 change much in either OFES2 and observations (Fig. 9a-d, Fig. S3a-d).

4 Interannual variations

4.1 Niño3.4 and Indian Ocean Dipole Mode indexes

We examine the monthly time series of indexes for El Niño and IOD events to determine how well OFES2 reproduces these variations over 1968-2016 (Fig. 10 and Table 2). HadISST version 1 (Rayner et al., 2003) is used as the reference because it covers the whole analysis period. In HadISST, however, the anomalous SST in the eastern pole during the IOD events, which is discussed in Section 4.2, appears to be obscure.

The variations in the Niño3.4 index are very similar between OFES2 and HadISST (Fig. 10a). The correlation of indexes between OFES2 and HadISST is very high (0.963), and its RMS amplitude of OFES2 (0.95 °C) is slightly larger than the observed value (0.89 °C). For IOD, the Dipole Mode Index (DMI) time series in OFES2 is also similar to that in HadISST (Fig. 10b). The correlation between the DMI of OFES2 and HadISST is high (0.714), but its RMS amplitude in OFES2 (0.52 °C) is considerably larger than that in HadISST (0.32 °C).

In OFES, the indexes of El Niño and IOD events are also similar to those in HadISST (see Table 2 for the correlations and RMS amplitudes), with somewhat lower correlations than OFES2. One possible cause for these high correlations in OFES2 is the replacement of atmospheric dataset by JRA55-do to estimate surface fluxes because usually SST in the ocean models is strongly constrained to the atmospheric data via the surface flux. The RMS amplitudes in OFES (0.93 °C for Niño3.4 index and 0.38 °C for DMI) are comparable to those of HadISST. The reason why the DMI RMS amplitude is larger in OFES2 (0.52 °C) than in OFES or the HadISST (0.32 °C) is the SSTA variations simulated in the eastern pole of the IOD. The SSTAs in the eastern pole in OFES2 are colder (warmer) mostly in the positive (negative) IOD years of 1982, 1983, 1994, 1997, and 2006 (1996, 1998, and 2010) than OFES and HadISST (Fig. 10c). The SSTA variations show that its amplitude in OFES2 (0.43 °C) is much larger than in OFES (0.33 °C) and HadISST (0.33 °C). On the other hand, OFES2 exhibits well the time series of observed SSTA in the western pole (Fig. 10d), with the correlation of the SSTA between OFES2 and HadISST being 0.847. This value is higher than 0.751 from OFES. In OFES, the warm biases increase greatly after 2005. The RMS amplitudes in OFES2 (0.31 °C) and HadISST (0.33 °C) are relatively small compared to that in OFES (0.41 °C). Therefore, we will closely examine this SST distribution around the eastern pole in the typical positive and negative IOD years next.

4.2 Sea surface temperature around the eastern pole of the Indian Ocean Dipole

We examine strong positive and negative IOD events in 1997 and 2010 as typical cases. The satellite observations captured a low SST (< 26 °C) in the nearshore area to the southwest of Sumatra and Java during the positive event (Fig. 11c). The anomalous southeasterly wind induces coastal upwelling, and therefore, the SST near the coast becomes low compared with the offshore SST. OFES2 (Fig. 11a) reproduces this observed anomalous cold SST along the coast well, although the SST near Java is too cold (< 22 °C). During the negative event, the satellite-observed SST was warm (~30 °C) to the west of Sumatra (Fig. 11g). OFES2 (Fig. 11e) also exhibits this observed warm SST well. This warming is presumably due to weak

upwelling from the weak wind west of Sumatra (Fig. 11e). OFES2 reproduces the cold and warm SST anomalies well in the eastern pole of these and other (Fig. S4) IOD events.

325   We used the DMI estimated from HadISST version 1 (Rayner et al. 2003) as the observational index because HadISST covers a long period: 1871 to the present. However, HadISST in Fig. 11d (Fig. 11h) is incapable of capturing the cold (warm) SST near the southwestern coast of Sumatra and Java in the typical positive (negative) IOD event. Therefore, the DMI amplitude from HadISST is likely to be too small. In contrast, OISST v2 (Reynolds 1988), covering the relatively short period from 1981 to the present, exhibits well the anomalous SST near the coast both in the positive and negative IOD events

330 (Fig. S5), which is similar to the satellite observations (Figs. 11c and 11g). The average amplitude of the DMI over 1981-2016 is 0.54 °C for OISST v2, which is comparable to 0.54 °C for OFES2. These results suggest that OFES2 reproduces the anomalous SST near the southwestern coast of Sumatra and Java during IOD events and exhibits both the variations in and the amplitudes of the DMI well.

    OFES (Fig. 11b) did not accurately reproduce the observed anomalous cold SST (Fig. 11c) near the Sumatra and Java

335 during the mature positive IOD event in 1997. The SST in OFES remains unrealistically warm (> 26 °C) to the southwest of Sumatra and Java. We attribute this fault to the wind stress driving OFES. The strong southeasterly wind stress (thick arrows, > 0.05 N m^{-2}) is located far offshore (Fig. 11b), which cannot induce coastal upwelling with realistic strength. On the other hand, the anomalous warm SST in the eastern pole during the negative IOD in 2010 is fairly realistic in OFES (Fig. 11f), although the SST in the entire region is somewhat colder than from the satellite observations (Fig. 11g). This cold SST bias

340 seems consistent with the bias all over the Indian Ocean in the long-term mean in OFES (Fig. 4b). These features generally apply to other IOD events (Fig. S4). The difference in the SST reproducibility in the eastern pole between the positive and negative events in OFES probably comes from the asymmetric property of the IOD events (e.g., Hong et al., 2008).

5 Summary and discussion

This paper describes a new version of our OGCM, which we call OFES2. OFES2 improves the atmospheric forcing to

345 include the diurnal cycle and now includes a tidal mixing scheme and a sea-ice model. We have presented how well OFES2 simulates the mean oceanic features and interannual variations such as El Niño and IOD events, which are generally improved compared to OFES (Table 3).

    OFES2 reproduces large-scale circulations, global distributions of mesoscale eddy activities, SSTs, and SSSs well with significant improvements found in the water properties in the subsurface in the subtropical Western Pacific and the Arabian

350 and Indonesian Seas over OFES. OFES2 also represents the large SSHA RMS accompanied by strong currents well, such as the Gulf Stream and the Kuroshio, which is too large in OFES. However, the RMS values are slightly smaller in most regions in OFES2 than in the satellite observations. The surface momentum fluxes in OFES2 are estimated with a bulk formula by using the surface wind relative to the simulated surface current. This method weakens mesoscale eddies, as Zhai and Greatbatch (2007) and Renault et al. (2019a) suggested, which possibly damps the SSHA RMS a bit too much in OFES2.

355   Considering the atmospheric response to the SST distributions, such as vertical mixing (e.g., Wallace et al., 1989) and pressure adjustment over the SST fronts (e.g., Lindzen and Nigam, 1987) in OGCM may be one of the solutions to overcome this issue. Renault et al. (2019b) also showed the imprints of surface currents on surface atmospheric winds through surface momentum flux in the satellite observations and coupled simulations. Sensitivity experiments on the coupling coefficients (Renault et al. 2020) remain as our near-future work.

360   The variations of the climate indexes of Niño3.4 and DMI are also well simulated in OFES2. The correlations of the monthly indexes between OFES2 and the observations are slightly higher than for OFES. During the typical positive IOD event, anomalous southeasterly wind near the Sumatra and Java induces anomalous cold SST fields via coastal upwelling. OFES2 reproduces this anomalous SST distribution well during typical events, which is due to the realistic surface winds of JRA55-do driving OFES2. In addition, the Atlantic Multidecadal Oscillation (AMO, Enfield et al. 2001) was examined,

365   although the period of OFES2 over 1958-2016 is rather short. The monthly AMO index in OFES2 varies with the observation with a correlation value of 0.90, which is much higher than 0.54 for OFES (Fig. 12). Other various climate variations are yet to be examined.

    There are several issues in OFES2 that remain unrealistic from OFES. For example, parts of the pathways of the Kuroshio and Gulf Stream are unrealistic, which created a strong SST bias (Fig. 4a and 4b) and unrealistic SSHA RMS variability (Fig.

370   5d and 5e) around these currents. OFES2 uses the wind velocity relative to the surface current to estimate the surface momentum fluxes and a deeper maximum bottom depth (7,500 m), as Tsujino et al. (2013) and Kurogi et al. (2016) did to solve these issues for the Kuroshio. Nevertheless, the simulated Kuroshio in OFES2 is frequently unrealistically detached from Kyushu. To simulate the realistic Gulf Stream separation, the importance of the sub-grid parameterization (Schoonover et al. 2016), adequate topographic resolution (Schoonover et al. 2017), ageostrophic circulation, front genesis (McWilliams

375   et al. 2019) were suggested. Chassignet and Xu (2017) also succeeded in simulating the separation in a simulation at a horizontal resolution of 1/50°. In OFES2, the unrealistic path way of the Gulf Stream makes significant biases in SST, SSS, and SSH. Sensitivity experiments similar to the previous studies are needed to overcome this problem in OFES2.

    The Azores Current was also not simulated even with a restoring condition to reproduce the impact of the salty Mediterranean outflow, which would establish the Azores Current as suggested in Jia et al. (2000). An interesting result is

380   that the Azores Current and the outflow do exist in the 1960s, but the both abruptly decay in the 1970s and disappear after the 1980s (see Figs. S6 and S7 for details). We have not yet found the cause of this behavior.

    The impacts of the Mediterranean outflow on the meridional overturning were also suggested by previous studies (e.g. Reid 1979, McCartney and Mauitzen 2001). The overturning circulation in the Atlantic Ocean in OFES2 (Fig. S8) appears realistic but more detailed examinations are needed to improve the Atlantic circulations in the whole depths. The salty

385   outflows into the Arabian Sea and the water mass properties in the Indonesian Seas are improved in OFES2 with the restoring of temperature and salinity near the straits and with the tidal mixing scheme, respectively. Obviously, there are more issues to investigate water mass properties in other regions in the future.

Another issue in OFES2 is that the domain does not include the polar regions in the latitudes higher than 76°. The sea-ice distribution is unrealistic in the Arctic region (Fig. 9e and 9g), whose decreasing trend is not also simulated. One possible reason for these defects is the existence of the northern boundary in OFES2 as discussed in Section 3.5. On the one hand, the meridional overturning circulations in the globe and Atlantic Ocean (Fig. S8) seem reasonable as mentioned above. A century-scale integration would be necessary to pursue this issue.

The latest supercomputer systems enable us to perform global eddying ocean simulations with much less computational cost than before. Sensitivity experiments are becoming more feasible. Sasaki et al. (2018) showed that the inclusion of a tidal mixing scheme can result in an enhancement in ITF transport due to the basin-scale SSH increase in the tropical Pacific Ocean. While the direct impact of tidal mixing is local, its impact appears to spread over a whole basin via Rossby and Kelvin waves (Furue et al. 2015). Ensemble simulations are another way of utilizing computational power. Nonaka et al. (2016) conducted a 3-member ensemble simulation using OFES, and they suggested the existence of intrinsic variations in the midlatitude ocean currents. One future direction of global, multidecadal, eddying ocean simulation is to obtain a large ensemble.

Global or basin-scale simulations capable of resolving oceanic submesoscales with a finer horizontal resolution (e.g., Sasaki et al. 2014, Qiu et al. 2018) are also being pursued. However, it is still difficult to execute these simulations over many decades due to the huge demands on computational resources and storage. The causes behind model biases in eddying simulations are still unresolved, and we still have much to learn from these simulations. Our improved hindcast simulation will be useful for exploring oceanic processes and for Lagrangian analyses of water mass properties (e.g., Kida et al., 2019). We hope that OFES2 will serve as a valuable tool for studying various oceanic features with wide spatiotemporal scales from mesoscale to large-scale circulation and from intraseasonal to decadal timescales.

Author contribution

H. Sasaki and S. Kida implemented a tidal scheme and N. Komori implemented a sea-ice model into OFES2. H. Sasaki, S. Kida, and R. Furue wrote the manuscript. H. Aiki, Y. Masumoto, T. Miyama, M. Nonaka, Y. Sasai, and B.Taguchi contributed model configurations and writing the manuscript.

Code and data availability

OFES and OFES2 are based on MOM3, which is available through https://github.com/mom-ocean/MOM3. The code has been modified for large-scale high performance simulation and implementations of sea-ice model and tidal mixing scheme. The modification is copyrighted by Japan Agency for Marine-Earth Science and Technology (JAMSTEC). The modified code, scripts, and input data to run OFES and OFES2 are available under a copyright agreement. Monthly fields from

OFES2 become available in the immediate future. Monthly fields from OFES can be downloaded from https://doi.org/10.17596/0002029.

We thank Hiroyuki Tsujino for providing us with the earlier version of the JRA55-do dataset before the official release of the latest version (https://esgf-node.llnl.gov/search/input4mips/). The river runoff dataset from CORE version 2 was downloaded from https://data1.gfdl.noaa.gov/nomads/forms/core/COREv2.html. The ocean bathymetry from ETOPO1 (doi:10.7289/V5C8276M) was used. WOA13 and WOA98 are available at https://www.nodc.noaa.gov/OC5/woa13/ and https://www.esrl.noaa.gov/psd/data/gridded/data.nodc.woa98.html, respectively. The HadISST was downloaded from https://www.metoffice.gov.uk/hadobs/hadisst/. AMSR-E SST version 7 and AVHRR SST version 4.1 were used through APDRC (http://apdrc.soest.hawaii.edu/index.php). The AMSR data are produced by Remote Sensing Systems and were sponsored by the NASA AMSR-E Science Team and the NASA Earth Science MEaSUREs Program. AVHRR Pathfinder SSTs were made by GHRSST and the US National Oceanographic Data Center. The AVISO SSH data and FES2012 tidal current speeds were downloaded through Aviso (ftp.access.aviso.altimetry.fr). The DMIs for HadISST were downloaded from http://www.jamstec.go.jp/aplinfo/sintexf/iod/dipole_mode_index.html.

Acknowledgements

OFES and OFES2 were conducted by using the Earth Simulator under the support of JAMSTEC. This work was supported by a Grant-in-Aid for Scientific Research on Innovative Areas 6102 (KAKENHI Grant No. JP19H05701) from JSPS of Japan. H. Sasaki and Y. Sasai were supported by JSPS KAKENHI (grant number 17K05662). S. Kida was supported by JSPS KAKENHI (grant number 18H03731). M. Nonaka was supported by JSPS KAKENHI (grant number 17K05665). We appreciate Takeshi Doi, who provided information about observational data to examine IOD events.

References

Adcroft, A., Hill, C., and Marshall, J.: Representation of topography by shaved cells in a height coordinate ocean model, Mon. Wea. Rev., 125(9), 2293–2315, doi:10.1175/1520-0493(1997)125<2293:ROTBSC>2.0.CO;2, 1997.

Amante, C. and Eakins, B. W.: ETOPO1 1 arc-minute global relief model: procedures, data sources and analysis. NOAA Technical Memorandum NESDIS NGDC-24, 19 pp, March 2009. http://www.ngdc.noaa.gov/mgg/global/global.html, 2009.

Aoki, K., Kubokawa, A., Furue, R. and Sasaki, H.: Influence of eddy momentum fluxes on the mean flow of the Kuroshio Extension in a 1/10° Ocean General Circulation Model, J. Phys. Oceanogr., 46 (9), 2769–2784, doi:10.1175/JPO-D-16-0021.1, 2016.

Carrère, L., Lyard, F., Cancet, M., Guillot, A., and Roblou, L.: FES 2012: a new global tidal model taking advantage of nearly 20 years of altimetry. In: Proceedings of meeting "20 Years of Altimetry", Venice, 2012

Chassignet, E. P., Hurlburt, H. E., Smedstad, O. M., Halliwell, G. R., Wallcraft, A. J., Metzger, E. J., Blanton B. O., Lozano, C., Rao, D. B., Hogan, P. J., and Srinivasan, A.: Generalized vertical coordinates for eddy-resolving global and coastal ocean forecasts, Oceanography, 19(1), 118–129. Doi:10.5670/oceanog.2006.95, 2006.

450 Chassignet, E.P. and Xu, X.: Impact of horizontal resolution (1/12° to 1/50°) on Gulf Stream separation, penetration, and variability. J. Phys. Oceanogr., 47, 1999–2021, doi:10.1175/JPO-D-17-0031.1, 2017.

Casey, K. S., Brandon, T. B., Cornillon, P., and Evans, R.: The past, present and future of the AVHRR Pathfinder SST program, in Oceanography from Space, edited by: Barale, V., Gower, J. F. R., and Alberotanza, L., Springer, doi:10.1007/978-90-481-8681-5_16, 2010.

455 Chelton, D. B., deSzoeke, R. A., Schlax, M. G., El Naggar, K., and Siwertz, N.: Geographical variability of the first baroclinic Rossby radius of deformation, J. Phys. Oceanogr., 28(3), 433–460. Doi:10.1175/1520-0485(1998)028<0433:GVOTFB>2.0.CO;2, 1998.

Chelton, D. B., Schlax, M. G., Samelson, R. M., and de Szoeke, R. A.: Global observations of large oceanic eddies, Geophys. Res. Lett., 34, L15606, doi:10.1029/2007GL030812, 2007.

460 Conkright, M.E., Levitus, S. O'Brien, T., Boyer, T. P., Stephens, C., Johnson, D., O. Baranova, Antonov, A., Gelfeld, R., Rochester, J., and Forgy, C.: World Ocean Database 1998 Documentation and Quality Control, National Oceanographic Data Center, Silver Spring, MD, 1998.

Enfield, D.B., Mestas-Nunez, A.M., and Trimble, P.J.: The Atlantic Multidecadal Oscillation and its relationship to rainfall and river flows in the continental U.S., Geophys. Res. Lett., 28 (10), 2077–2080, doi: 10.1029/2000GL012745, 2001.

465 Ffield, A., and Gordon, A. L.: Tidal mixing signatures in the Indonesian Seas, J. Phys. Oceanogr., 26(9), 1924–1937, doi:10.1175/1520-0485(1996)026<1924:TMSITI>2.0.CO;2, 1996.

Furue, R., Jia, Y., McCreary, J. P., Schneider, N., Richards, K. J., Müller, P., Cornuelle, B. D., Avellaneda, N. M., Stammer, D., Liu, C., and Köhld, A.: Impacts of regional mixing on the temperature structure of the equatorial Pacific Ocean. Part 1: Vertically uniform vertical diffusion, Ocean Modell., 91, 91–111, doi.org:10.1016/j.ocemod.2014.10.002, 2015.

470 Hibler III, W. D.: A dynamic thermodynamic sea ice model, J. Phys. Oceanogr., 9(4), 815–846, doi:10.1175/1520-0485(1979)009<0815:ADTSIM>2.0.CO;2, 1979.

Hong, C., Li, T., LinHo, and Kug, J.: Asymmetry of the Indian Ocean Dipole. Part I: Observational analysis, J. Clim., 21(18), 4834–4848, doi:10.1175/2008JCLI2222.1, 2008.

Hosoda, S., Ohira, T., and Nakamura, T.: A monthly mean dataset of global oceanic temperature and salinity derived from 475 Argo float observations. JAMSTEC Report of Research and Development, 8, 47–59, doi:10.5918/jamstecr.8.47, 2008.

Hu, S., Sprintall, J., Guan, C., Sun, B., Wang, F., Yang, G., Jia, F., Wang, J., Hu, D., and Chai, F.: Spatiotemporal features of intraseasonal oceanic variability in the Philippine Sea from mooring observations and numerical simulations, J. Geophys. Res.: Oceans, 123 (7), 4874– 4887, doi:10.1029/2017JC013653, 2018.

Hunke, E. C., and Dukowicz, J. K.: The elastic–viscous–plastic sea ice dynamics model in general orthogonal curvilinear coordinates on a sphere—Incorporation of metric terms, Mon. Wea. Rev., 130(7), 1848–1865. doi:10.1175/1520-0493(2002)130<1848:TEVPSI>2.0.CO;2, 2002.

Jayne, S. R., and St. Laurent, L. C.: Parameterizing tidal dissipation over rough topography, Geophys. Res. Lett., 28(5), 811–814, doi:10.1029/2000GL012044, 2001.

Jia, Y. (2000). Formation of an Azores Current due to Mediterranean overflow in a modeling study of the North Atlantic, J. Phys. Oceanogr., 30(9), 2342–2358, doi:10.1175/1520-0485(2000)030<2342:FOAACD>2.0.CO;2, 2000.

Jungclaus, J. H., Fischer, N., Haak, H., Lohmann, K., Marotzke, J., Matei, D., Mikolajewicz, U., Notz, D., and Storch, J. S.: Characteristics of the ocean simulations in MPIOM, the ocean component of the MPI-Earth system model, J. Adv. Model. Earth Syst., 5(2), 422–446, doi:10.1002/jame.20023, 2013.

Kalnay, E., Kanamitsu, M., Kistler, R., Collins, W., Deaven, D., Gandin, L., Iredell, M., Saha, S., White, G., Woollen, J., Zhu, Y., Chelliah, M., Ebisuzaki, W., Higgins, W., Janowiak, J., Mo, K. C., Ropelewski, C., Wang, J., Leetmaa, A., Reynolds, R., Jenne, R., and Joseph, D.: The NCEP/NCAR 40-year reanalysis project, Bull. Amer. Meteor. Soc., 77(3), 437–471, doi:10.1175/1520-0477(1996)077<0437:TNYRP>2.0.CO;2, 1996.

Kaplan, A., Cane, M., Kushnir, Y., Clement, A., Blumenthal, M., and Rajagopalan, B.: Analyses of global sea surface temperature 1856-1991, J. Geophys. Res., 103 (C9), 18567-18589, doi:10.1029/97JC01736, 1998.

Kida, S., Price, J. F., and Yang, J.: The upper-oceanic response to overflows: A mechanism for the Azores Current, J. Phys. Oceanogr., 38(4), 880–895, doi:10.1175/2007JPO3750.1, 2008.

Kida, S., Richards, K. J., and Sasaki, H.: The fate of surface freshwater entering the Indonesian Seas, J. Geophys. Res.: Oceans, 124(5), 3228–3245, doi: 10.1029/2018JC014707, 2019.

Kwok, R., Cunningham, G. F., and Pang, S. S.: Fram Strait sea ice outflow, J. Geophys. Res., 109 (C1), C01009, doi:10.1029/2003JC001785, 2004.

Kobayashi, S., Ota, Y., Harada, Y., Ebita, A., Moriya, M., Onoda, H., Onogi, K., Kamahori, H., Kobayashi, C., Endo, H., Miyaoka, K., and Takahashi, K.: The JRA-55 reanalysis: General specifications and basic characteristics. J. Meteorol. Soc. of JPN Ser. II, 93(1), 5–48, doi:10.2151/jmsj.2015-001, 2015.

Koch-Larrouy, A., Madec, G., Bouruet-Aubertot, P., Gerkema, T., Bessières, L., and Molcard, R.: On the transformation of Pacific Water into Indonesian Throughflow Water by internal tidal mixing, Geophys. Res. Lett., 34, L04604, doi:10.1029/2006GL028405, 2007.

Komori, N., Takahashi, K., Komine, K., Motoi, T., Zhang, X., and Sagawa, G.: Description of sea-ice component of coupled ocean sea-ice model for the earth simulator (OIFES), J. Earth Simulator, 4, 31–45, https://www.jamstec.go.jp/ceist/j/publication/journal/jes_vol.4/pdf/JES4_24_komori.pdf, 2005.

Kurogi, M., Tanaka, Y., and Hasumi, H.: Effects of deep bottom topography on the Kuroshio Extension studied by a nested-grid OGCM, CLVAR Exchanges, 69 (20), 19–21, http://www.clivar.org/sites/default/files/documents/Exchanges_69.pdf, 2016.

Kutsuwada, K.: Impact of wind/wind-stress field in the North Pacific constructed by ADEOS/NSCAT data, J. Oceanogr., 54(5), 443–456, doi:10.1007/BF02742447, 1998.

515 Kutsuwada, K., Kakiuchi, A., Sasai, Y., and Sasaki, H.: Wind-driven North Pacific Tropical Gyre using high-resolution simulation outputs, J. Oceanogr., 75 (1), 81–93, doi:10.1007/s10872-018-0487-8, 2019.

Large W., and Yeager S.: Diurnal to decadal global forcing for ocean and sea-ice models: The data sets and flux climatologies, NCAR Technical Note NCAR/TN-460+STR, doi:10.5065/D6KK98Q6, 2004.

Large, W. G., McWilliams, J. C., and Doney, S. C.: Oceanic vertical mixing: A review and a model with a nonlocal
520 boundary layer parameterization, Rev. Geophys., 32(4), 363– 403, doi:10.1029/94RG01872, 1994.

Lindzen, R. S. and Nigam, S.: On the role of sea surface temperature gradients in forcing low-level winds and convergence in the tropics, J. Atmos. Sci., 44(17), 2418–2436, doi:10.1175/1520-0469(1987)044<2418:OTROSS>2.0.CO;2, 1987.

Locarnini, R. A., Mishonov, A. V., Antonov, J. I., Boyer, T. P., Garcia, H. E., Baranova, O. K., Zweng, M. M., Paver, C. R., Reagan, J. R., Johnson, D. R., Hamilton, M., and Seidov, D.: World Ocean Atlas 2013, Volume 1: Temperature. S.
525 Levitus, Ed., A. Mishonov Technical Ed.; NOAA Atlas NESDIS 73, 40 pp, doi:10.7289/V55X26VD, 2013.

McWilliams, J.C., Gula, J., and Molemaker, M.J.: The Gulf Stream North wall: Ageostrophic circulation and frontogenesis, J. Phys. Oceanogr., 49, 893–916, https://doi.org/10.1175/JPO-D-18-0203.1, 2019.

Maltrud, M. E. and McClean, J. L.: An eddy resolving global 1/10° ocean simulation, Ocean Modelling, 8 (1–2), 31–54, doi:10.1016/j.ocemod.2003.12.001, 2005.

530 Masumoto, Y.: Sharing the results of a high-resolution ocean general circulation model under a multi-discipline framework—a review of OFES activities, Ocean Dyn., 60 (3), 633–652, doi:10.1007/s10236-010-0297-z, 2010.

Masumoto, Y., Sasaki, H., Kagimoto, T., Komori, N., Ishida, A., Sasai, Y., Miyama, T., Motoi, T., Mitsudera, H., Takahashi, k., Sakuma, H., and Yamagata, T.: A fifty-year eddy-resolving simulation of the world ocean—Preliminary outcomes of OFES (OGCM for the Earth Simulator), J. Earth Simulator, 1, 35–56, doi:10.32131/jes.1.35, 2004.

535 Masumoto, Y., Morioka, Y., and Sasaki, H.: High-resolution Indian Ocean simulations – Recent advances and issues from OFES-.In Ocean Modeling in an Eddying Regime, edited by: Hecht, M. W., Hasumi, H., Geophysical Monograph Series, 177, AGU, Washington D.C., 165–175. doi:10.1029/177GM14, 2008.

McCartney, M.S., Mauritzen, C.: On the origin of the warm inflow to the Nordic Seas, Prog. Oceanogr. 51 (1), 125–214, doi:10.1016/S0079-6611(01)00084-2, 2001.

540 Nagai, T., Hibiya, T., and Bouruet-Aubertot, P.: Nonhydrostatic simulations of tide-induced mixing in the Halmahera Sea: A possible role in the trans formation of the Indonesian Throughflow waters, J. Geophys. Res.: Oceans, 122, 8933–8943, doi:10.1002/2017JC013381, 2017.

Nakamura, T., Toyoda, T., Ishikawa, Y., and Awaji, T.: Enhanced ventilation in the Okhotsk Sea through tidal mixing at the Kuril Straits, Deep Sea Res. PT I: Oceanogr. Res. Pap., 53 (3), 425–448, doi:10.1016/j.dsr.2005.12.006, 2006.

545 Nakano, T., Kitamura, T., Sugimoto, S., Suga, T., and Kamachi, M.: Long-term variations of North Pacific Tropical Water along the 137°E repeat hydrographic section, J. Oceanogr., 71 (3), 229–238, doi:10.1007/s10872-015-0279-3, 2005.

Noh, Y. and Kim, H. J.: Simulations of temperature and turbulence structure of the oceanic boundary layer with the improved near-surface process, J. Geophys. Res., 104 (C7), 15621–15634, doi:10.1029/1999JC900068, 1999.

Nonaka, M., Sasai, Y., Sasaki, H., Taguchi, B., and Nakamura, H.: How potentially predictable are midlatitude ocean currents?, Scientific Reports, 6, 20153. doi:10.1038/srep20153, 2016.

Pacanowski, R. C. and Griffies, S. M.: The MOM3 manual. GFDL Ocean Group Tech. Rep. 4, NOAA. Geophysical Fluid Dynamics Laboratory, Princeton, NJ., https://www.gfdl.noaa.gov/wp-content/uploads/files/model_development/ocean/mom3_manual.pdf, 1999.

Prasad, T. G., Ikeda, M., and Kumar, S.P.: Seasonal spreading of the Persian Gulf Water mass in the Arabian Sea, J. Geophys. Res.: Oceans, 106 (C8), 17059–17071, doi:10.1029/2000JC000480, 2001.

Qiu, B. and Chen, S.: Eddy-mean flow interaction in the decadally-modulating Kuroshio Extension system, Deep Sea Res. PT II: Trop. Stud. Oceanogr., 57, 1098–1110, doi:10.1016/j.dsr2.2008.11.036, 2010.

Qiu, B., Chen, S., Klein, P., Wang, J., Torres, H., Fu, L., and Menemenlis, D.: Seasonality in transition scale from balanced to unbalanced motions in the world ocean, J. Phys. Oceanogr., 48 (3), 591–605, doi:10.1175/JPO-D-17-0169.1, 2018.

Rayner, N. A., Parker, D. E., Horton, E. B., Folland, C. K., Alexander, L. V., Rowell, D. P., Kent, E. C., and Kaplan, A. (2003). Global analyses of sea surface temperature, sea ice, and night marine air temperature since the late nineteenth century, J. Geophys. Res.: Atmos., 108 (D14), 4407, doi:10.1029/2002JD002670, 2003.

Reid, J.L.: On the contribution of the Mediterranean Sea outflow to the Norwegian-Greenland Sea, Deep Sea Res. A. Oceanogra. Res. Pap., 26 (11), 1199–1223, doi:10.1016/0198-0149(79)90064-5, 1979.

Renault, L., McWilliams, J.C., and Penven, P.: Modulation of the Agulhas current retroflection and leakage by oceanic current interaction with the atmosphere in coupled Simulations. J. Phys. Oceanogr., 47 (8), 2077–2100, doi:10.1175/JPO-D-16-0168.1, 2017.

Renault, L., Marchesiello, P., Masson, S., and McWilliams, J. C.: Remarkable control of western boundary currents by eddy killing, a mechanical air-sea coupling process, Geophys. Res. Lett., 46 (5), 2743–2751, doi:10.1029/2018GL081211, 2019a.

Renault, L., Masson, S., Oerder, V., Jullien, S., and Colas, F.: Disentangling the mesoscale ocean-atmosphere interactions. J. Geophys. Res. Oceans, 124 (3) , 2164–2178, doi:10.1029/2018JC014628, 2019b.

Renault, L., Masson, S., Arsouze, T., Madec, G., and McWilliams, J. C.: Recipes for how to force oceanic model dynamics, J. Adv. Mod. Ear. Sys., 12 (2), e2019MS001715, doi:10.1029/2019MS001715, 2020.

Reynolds, R. W.: A real-time global sea surface temperature analysis, J. Clim., 1 (1), 75–86, doi:10.1175/1520-0442(1988)001<0075:ARTGSS>2.0.CO;2, 1988.

Roemmich, D., Johnson, G., Riser, S., Davis, R., Gilson, J., Owens, W. B., Garzoli, S. L., Schmid, C., and Ignaszewski, M. (2009). The Argo program: Observing the global ocean with profiling floats. Oceanography, 22 (2), 34–43, doi: 10.5670/oceanog.2009.36, 2009.

580   Rosati, A. and Miyakoda, K.: A general circulation model for upper ocean circulation, J. Phys. Oceanogr., 18 (11), 1601–1626, doi:10.1175/1520-0485(1988)018<1601:AGCMFU>2.0.CO;2, 1988.

Saji, N. H., Goswami, B. N., Vinayachandran, P. N., and Yamagata, T.: A dipole mode in the tropical Indian Ocean, Nature, 401 (6751), 360, doi:10.1038/43854, 1999.

Sasaki, H., Sasai, Y., Nonaka, M., Masumoto, Y., and Kawahara, S.: An eddy-resolving simulation of the quasi-global ocean
585   driven by satellite-observed wind field: Preliminary outcomes from physical and biological fields, J. Earth Simulator, 6, 35–49, https://www.jamstec.go.jp/ceist/j/publication/journal/jes_vol.6/pdf/JES6_24-Sasaki.pdf, 2006.

Sasaki, H., Nonaka, M., Masumoto, Y., Sasai, Y., Uehara, H., and Sakuma, H.: An eddy-resolving hindcast simulation of the quasiglobal ocean from 1950 to 2003 on the Earth Simulator, edited by Hamilton, K., Ohfuchi, W., High Resolution Numerical Modelling of the Atmosphere and Ocean, Springer, New York, NY, 157–186. https://doi.org/10.1007/978-0-
590   387-49791-4_10, 2008.

Sasaki, H., Klein, P., Qiu, B., and Sasai, Y. (2014). Impact of oceanic scale-interactions on the seasonal modulation of ocean dynamics by the atmosphere. Nature Communications, 5, 5636, doi:10.1038/ncomms6636, 2014.

Sasaki, H., Kida, S., Furue, R., Nonaka, M., and Masumoto, Y.: An increase of the Indonesian Throughflow by internal tidal mixing in a high-resolution quasi-global ocean simulation, Geophys. Res. Lett., 45 (16), 8416–8424,
595   doi:10.1029/2018GL078040, 2018.

Sasaki, Y. N. and Schneider, N.: Decadal shifts of the Kuroshio Extension jet: application of thin–jet theory, J. Phys. Oceanogr., 41, 979–993, doi:10.1175/2011JPO4550.1, 2011.

Schoonover, J., Dewar, W., Wienders, N., Gula, J., McWilliams, J.C., Molemaker, M.J., Bates, S.C., Danabasoglu, G.and Yeager, S.: North Atlantic barotropic vorticity balances in numerical models, J. Phys. Oceanogr., 46 (1), 289–303,
600   doi:10.1175/JPO-D-15-0133.1, 2016.

Schoonover, J., Dewar, W., Wienders, and Deremble, B.: Local sensitivities of the Gulf Stream separation, J. Phys. Oceanogr., 47 (2), 353–373, doi:10.1175/JPO-D-16-0195.1, 2017.

Sofianos, S. S. and Johns, W. E.: An Oceanic General Circulation Model (OGCM) investigation of the Red Sea circulation, 1, Exchange between the Red Sea and the Indian Ocean, J. Geophys. Res.: Oceans, 107 (C11), 3196,
605   doi:10.1029/2001JC001184, 2002.

St. Laurent, L. C., Simmons, H. L., and Jayne, S. R.: Estimating tidally driven mixing in the deep ocean, Geophys. Res. Lett., 29 (23), 2106, doi:10.1029/2002GL015633, 2002.

Taguchi, B., Schneider, N., Nonaka, M, and Sasaki, H.: Decadal variability of upper-ocean heat content associated with meridional shifts of western boundary current extensions in the North Pacific, J. Clim., 30, 6247–6264,
610   doi:10.1175/JCLI-D-16-0779.1, 2017.

Tanaka, Y., Hibiya, T., and Niwa, Y.: Estimates of tidal energy dissipation and diapycnal diffusivity in the Kuril Straits using TOPEX/POSEIDON altimeter data, J. Geophys. Res.: Oceans, 112 (C10), C10021, doi:10.1029/2007JC004172, 2007.

Tanaka, Y., Hibiya, T., and Niwa, Y.: Assessment of the effects of tidal mixing in the Kuril Straits on the formation of the North Pacific Intermediate Water, J. Phys. Oceanogr., 40 (12), 2569–2574, doi:10.1175/2010JPO4506.1, 2010.

Tsujino, H., Nishikawa, S., Sakamoto, K., Usui, N., Nakano, H., and Yamanaka, G.: Effects of large-scale wind on the Kuroshio path south of Japan in a 60-year historical OGCM simulation, Clim. Dyn., 41, 2287–2318, doi:10.1007/s00382-012-1641-4, 2013.

Tsujino, H., Urakawa, S., Nakano, H., Small, R. J., Kim, W. M., Yeager, S. G., Danabasoglu, G., Suzuki, T., Bamber, J. L., Bentsen, M., Böning, C. W., Bozec, A., Chassignet, E. P., Curchitser, E., Dias, F. B., Durack, P. J., Griffies, S. M., Harada, Y., Ilicak, M., Josey, S. A., Kobayashi, C., Kobayashi, S., Komuro, Y., Large, W. G., Le Sommer, J., Marsland, S. J., Masina, S., Scheinert, M., Tomita, H., Valdivieso, M., Yamazaki, D.: JRA-55 based surface dataset for driving ocean–sea-ice models (JRA55-do), Ocean Modell., 130, 79–139, doi:10.1016/j.ocemod.2018.07.002, 2018.

Wallace, J. M., Michell, T. P., and Deser, C.: The influence of sea-surface temperature on surface wind in the eastern equatorial Pacific: Seasonal and interannual variability, J. Clim., 2 (12), 1492–1499, doi:10.1175/1520-0442(1989)002<1492:TIOSST>2.0.CO;2, 1989.

Wentz, F. J. and Meissner, T.: Supplement 1: Algorithm theoretical basis document for AMSR-E ocean algorithms, Remote Sensing Systems Tech. Rep. 051707, 6 pp, http://images.remss.com/papers/rsstech /2007_051707_Wentz_AMSR_Ocean_V2_Supplement_1.pdf, 2007.

Zhai, X. and Greatbatch, R. J.: Wind work in a model of the northwest Atlantic Ocean, Geophys. Res. Lett., 34 (4), L04606, doi:10.1029/2006GL028907, 2007.

Zhai, X., Greatbatch, R. J., and Kohlmann, J. D.: On the seasonal variability of eddy kinetic energy in the Gulf Stream region, Geophys. Res. Lett., 35, L24609, doi:10.1029/2008GL036412, 2008.

Zweng, M. M., Reagan, J. R., Antonov, J. I., Locarnini, R. A., Mishonov, A. V., Boyer, T. P., Garcia, H. E., Baranova, O. K., Johnson, D. R., Seidov, D., and Biddle, M. M.: World Ocean Atlas 2013, Volume 2: Salinity. S. Levitus, Ed., A. Mishonov Technical Ed.; NOAA Atlas NESDIS 74, 39 pp, doi:10.7289/V5251G4D, 2013.
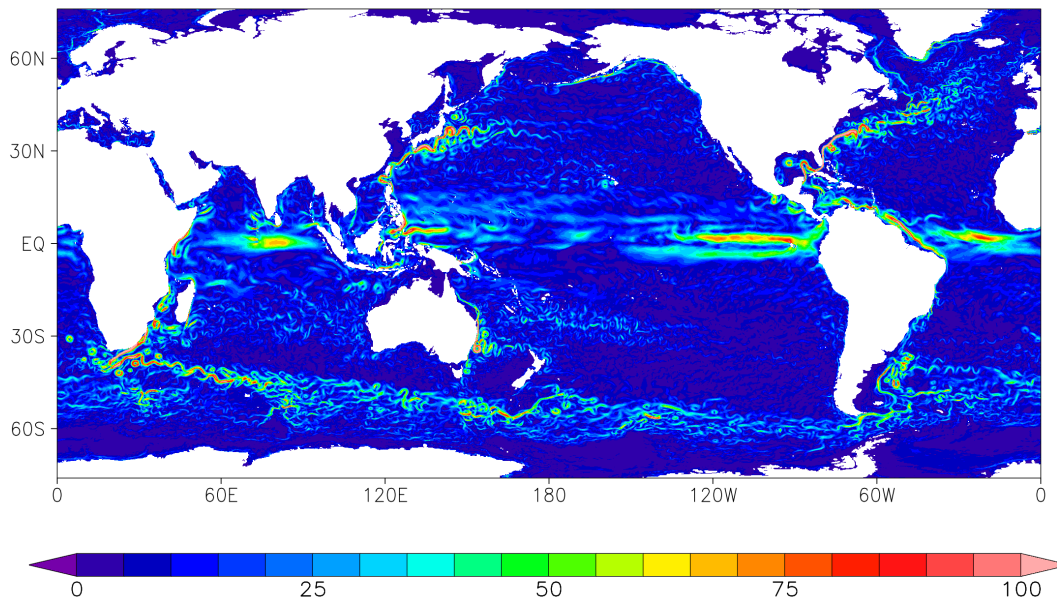
640

Figure 1: An example of monthly averaged surface current speeds (cm s^{-1}) in OFES2.
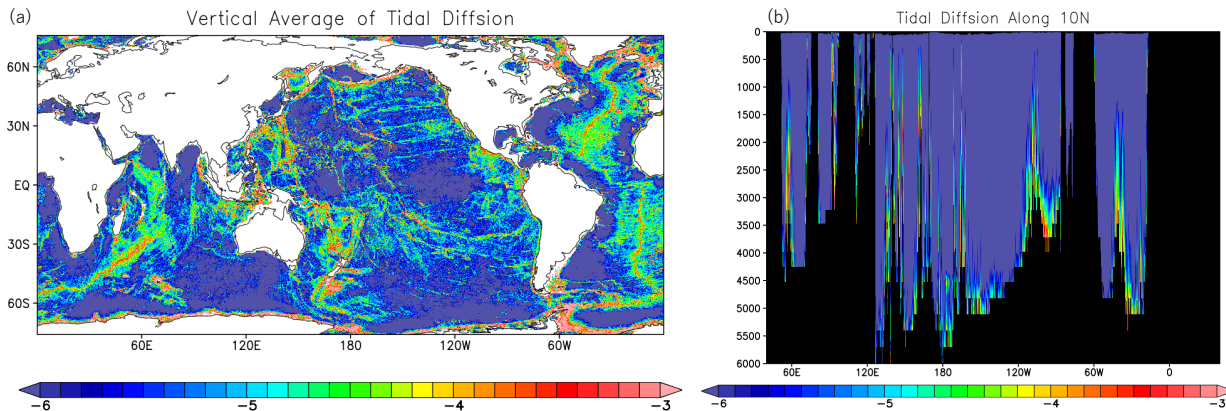
Figure 2: Daily mean vertical diffusivity (log10 m^2 s^{-1}) on December 1, 2016 estimated by the tidal mixing scheme (a) vertically
645 **averaged from the surface to the bottom and (b) in the vertical section along 10° N.**
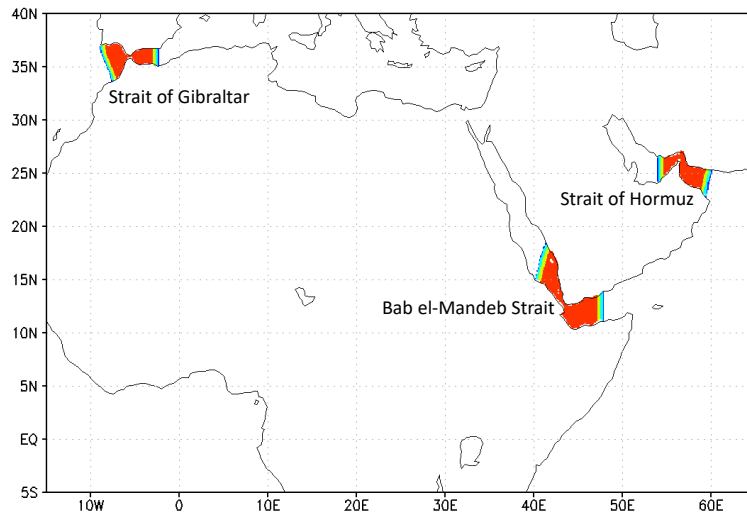
Figure 3: Timescales for restoring the temperature and salinity in and near the Straits of Gibraltar, Hormuz, and Bab el-Mandeb. Red, yellow, light blue, and blue represent timescales of 1, 5, 10, and 30 days, respectively.
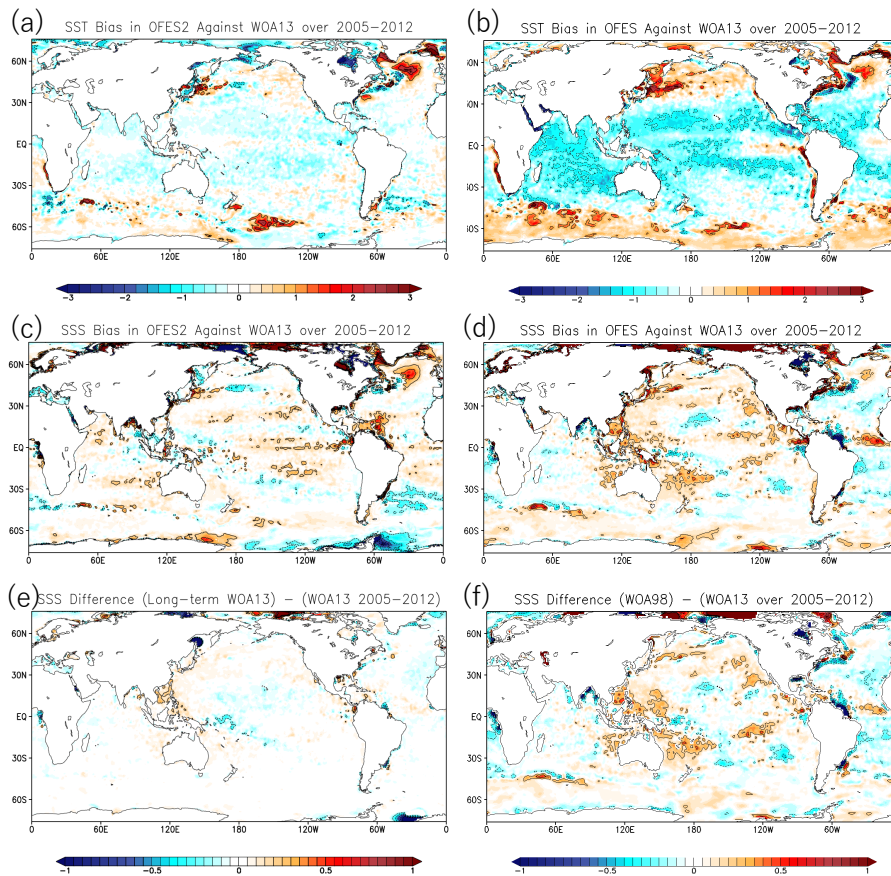
Figure 4: SST bias (°C) in (a) OFES2 and (b) OFES averaged over 2005-2012 against WOA13. (c) and (d) are the same as in (a) and (b), respectively, but the SSS bias is shown instead (psu). SSS differences in (e) long-term WOA13 and (f) WOA98 from WOA13 averaged over 2005-2012. The contour lines are superimposed at an interval of 1 °C for SST and 0.2 psu for SSS, but zero contour lines are omitted.
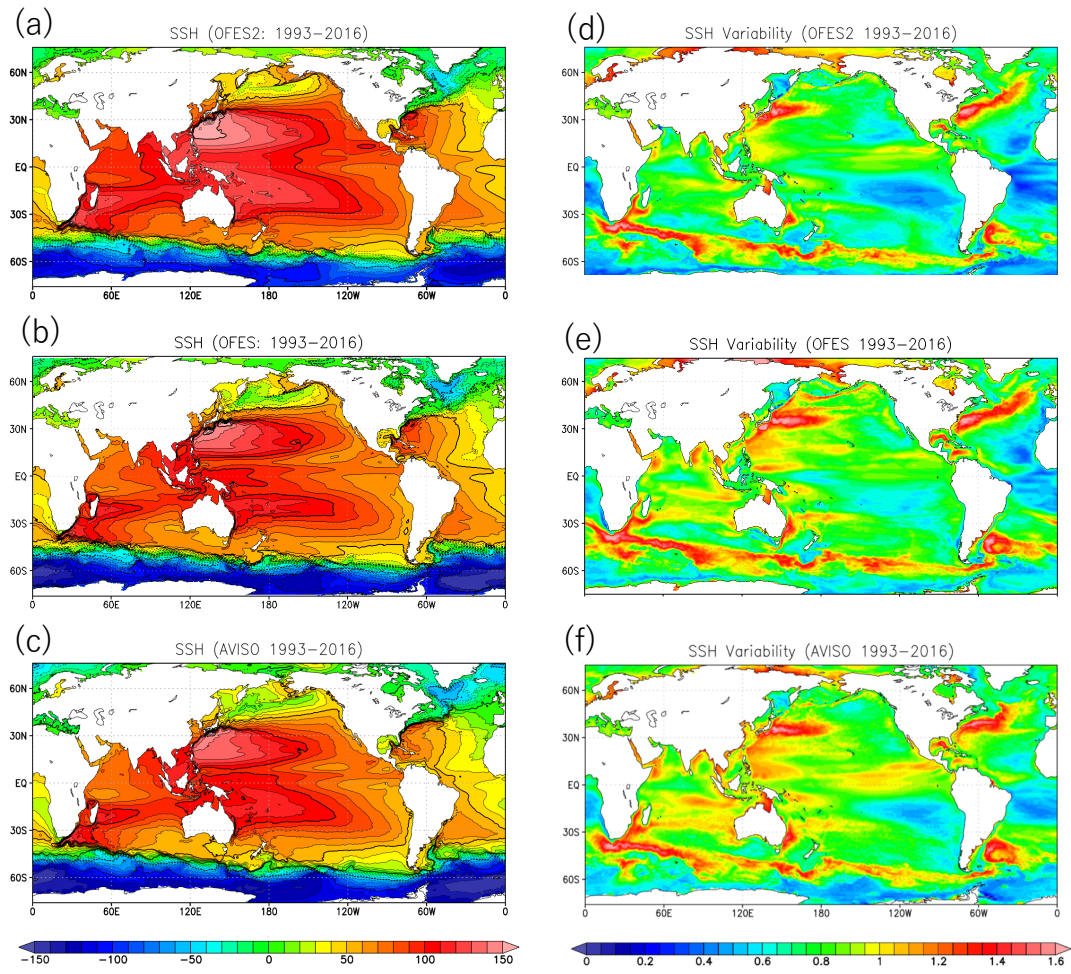
Figure 5: Mean (a, b, c) SSH (cm) and (d, e, f) its standard deviation (log10 cm) averaged over 1993-2016 from (a, d) OFES2, (b, e) OFES, and (c, f) AVISO observations. The SSH in OFES2 and OFES was offset by adding 50 cm.

655
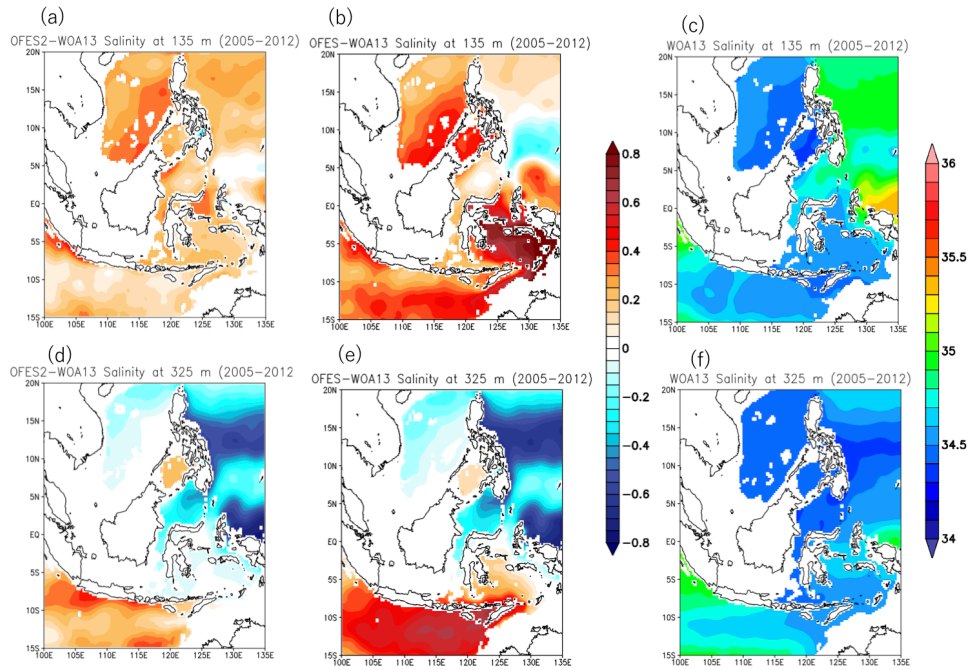
Figure 6: Salinity biases (a, b, d, e) against WOA13 (c, f) in OFES2 (a, d), OFES (b, e) at 135 m (a, b, c) and at 325 m (d, e, f). All fields are averaged over 2005-2012, and the units are psu.
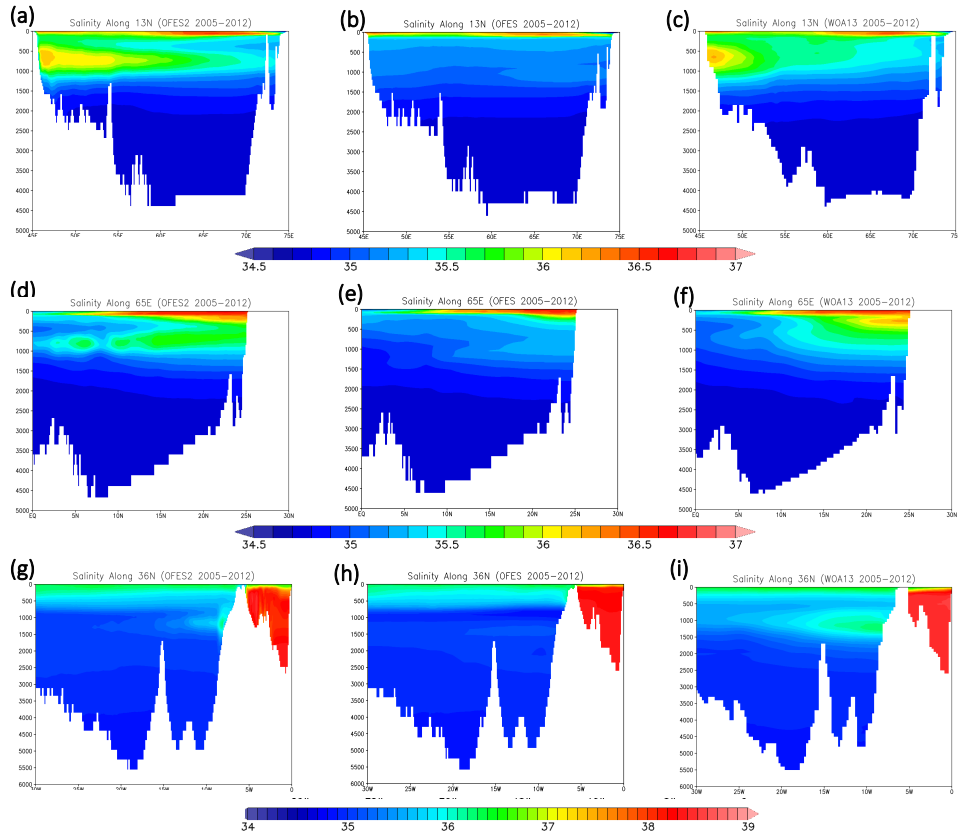
660

Figure 7: Vertical sections of mean salinity along (a-c) 13° N and (d-f) 65° E in the Arabian Sea and (g-i) 36° N in the eastern Atlantic Ocean averaged over 2005-2012: (a, d, g) OFES2, (b, e, h) OFES, and (c, f, i) WOA13.
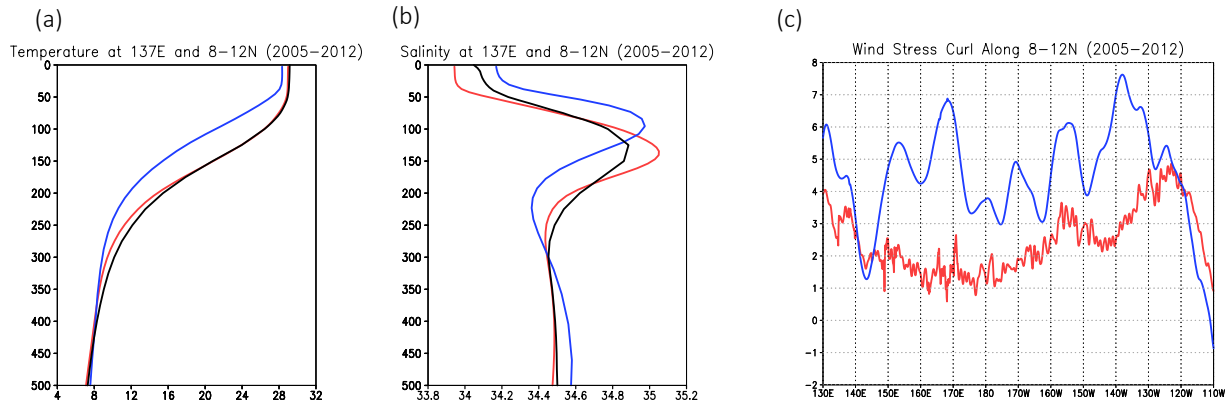
Figure 8: Vertical profile of (a) temperature (°C) and (b) salinity (psu) at 137°E averaged from 8°N to 12°N and over 2005–2012.

665 **(c) Longitudinal distributions of the wind stress curl (10^{-8} N m^{-3}) along 10° N (averaged from 8° N to 12° N and over 2005-2012). The red, blue, and black curves are OFES2 driven by JRA55-do, OFES driven by NCEP reanalysis, and the WOA13 observations, respectively.**
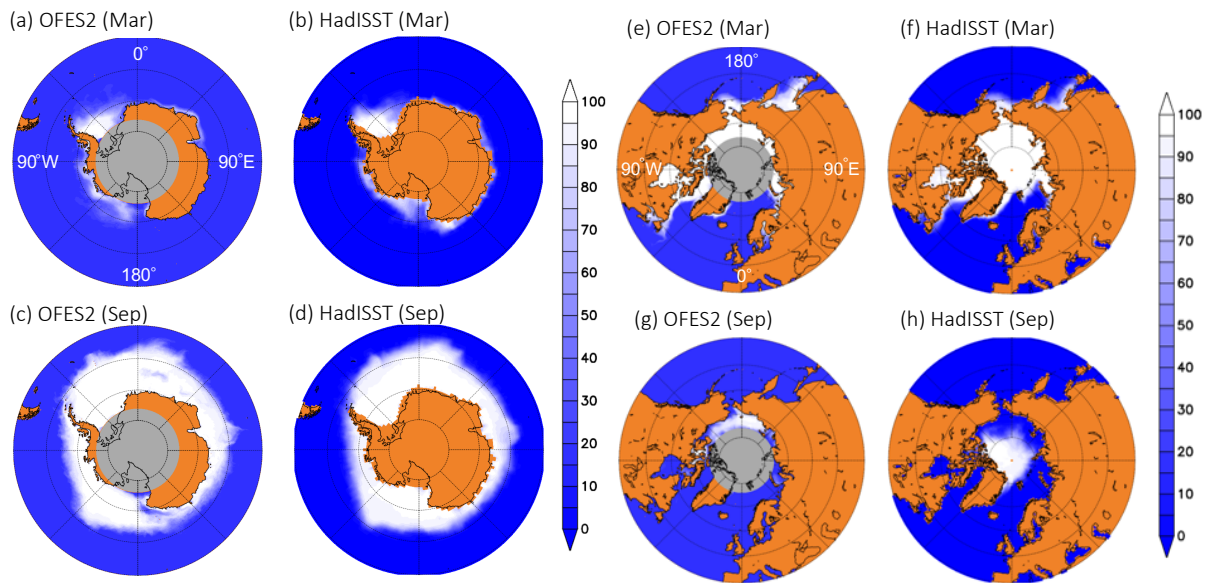
Figure 9: Sea-ice concentrations (%) in the Antarctic Ocean in (a, b) March and (c, d) September in (a, c) OFES2 and (b, d) HadISST averaged over 2005-2012. Similarly, the sea-ice concentrations in Arctic Ocean in (e, f) March and (g, h) September in (e, g) OFES2 and (f, h) HadISST. The gray areas are out of the model domain in OFES2 (a, c, e, g).
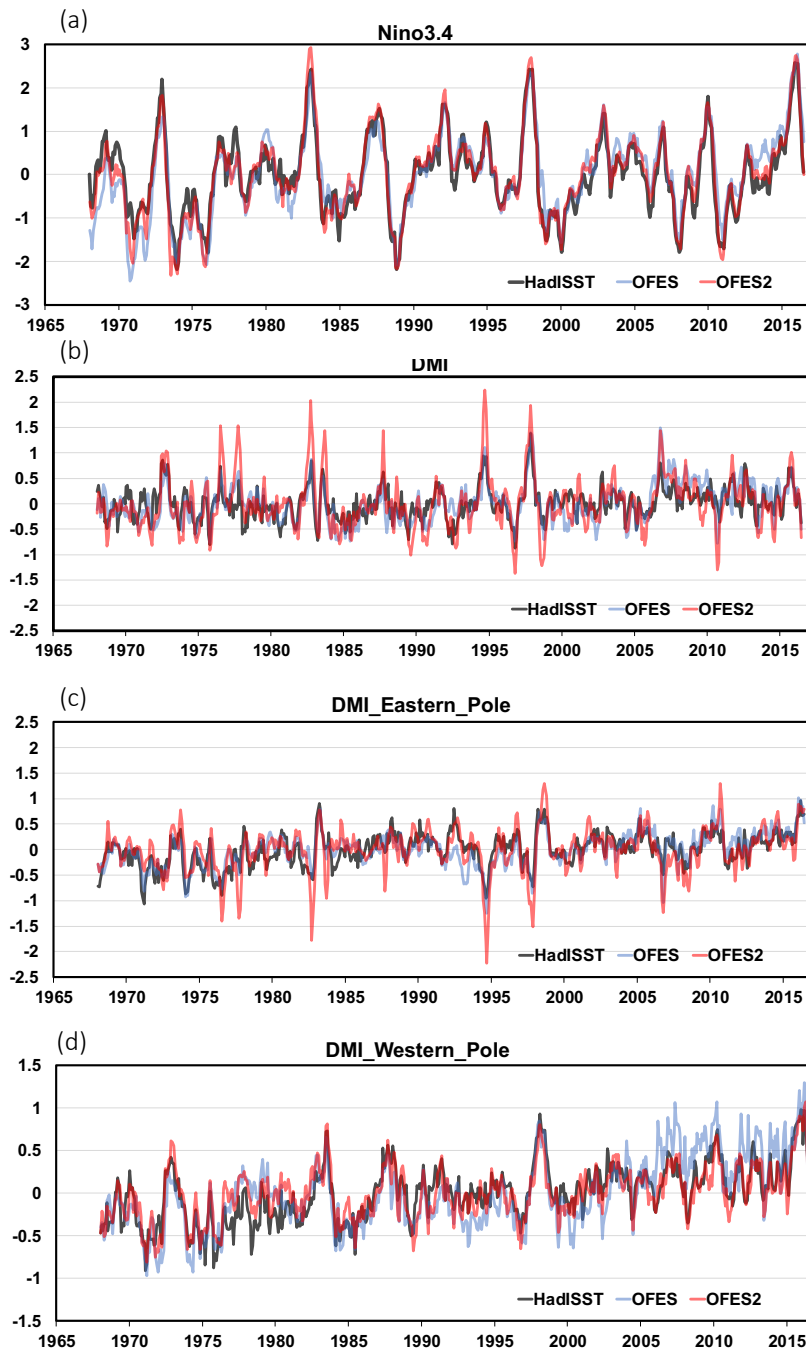
Figure 10: (a) Monthly Niño3.4 index defined as SSTAs (°C) in 165°-145° W and 5° S-5° N in the eastern topical Pacific and (b) the monthly DMI (°C) defined as difference between the SSTAs (°C) in the (c) eastern (90° E-110° E, 10° S-0°) and (d) the western (50°-70° E and 10° S-10° N) poles (Saji et al. 1999) from OFES2 (red curve), OFES (blue curve), and HadISST version 1 (http://www.cpc.ncep.noaa.gov/data/indices/ and http://www.jamstec.go.jp/frcgc/research/d1/iod/iod/dipole_mode_index.html).
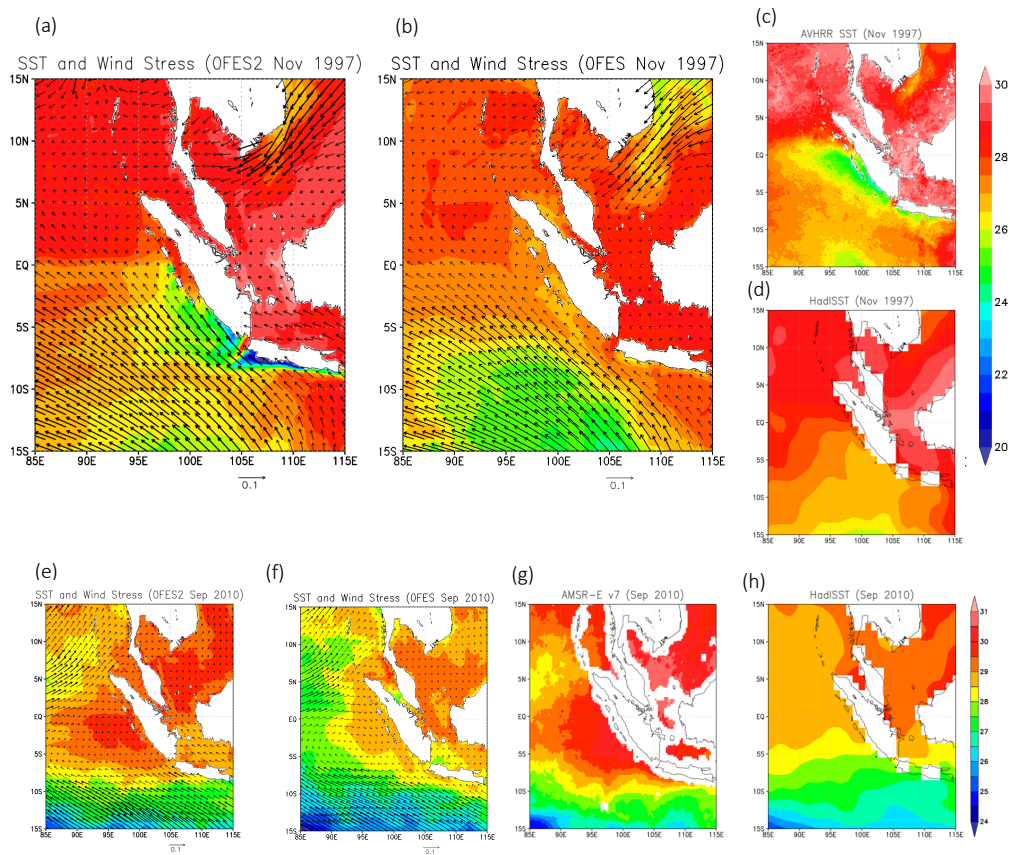
Figure 11: SST (°C) in a region including the IOD eastern pole (90°-110° E and 10° S-0°) in the mature month of (a-d) the 1997 positive IOD event (November 1997) and (e-h) the 2010 negative IOD event (September 2010). (a, e) OFES2, (b, f) OFES, (c, g) satellite observations of AVHRR version 4.1 (Casey et al. 2010) and AMSR-E version 7 (Wentz & Meissner 2007), and (d, h) HadISST ver.1 (Rayner et al. 2003). The vectors in (a, b, e, f) are the surface wind stress (N m-2) in the models, which are plotted at a 1°×1° resolution. The thick vectors denote wind stress magnitudes stronger than 0.05 N m-2.

680
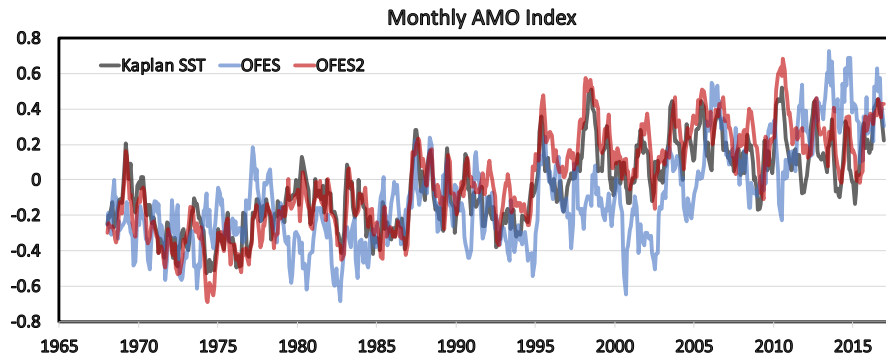
Figure 12: Monthly AMO index defined as SSTAs (°C) in 0° S-70° N in the eastern topical Pacific in the Kaplan SST (black curve, Kaplan et al. 1998), OFES2 (red curve), and OFES (blue curve).

	OFES2	OFES
Domain	76°S-76°N	75°S-75°N
Horizontal Resolution	0.1°	0.1°
Number of Vertical Levels	105	54
Maximum Depth	7,500 m	6,065 m
Bathymetry Data	ETOPO1	OCCAM 30'
Sea-Ice Model	Komori et al. 2005	-
Horizontal Mixing Scheme	Biharmonic	Biharmonic
Vertical Mixing Scheme	Noh & Kim 1999	KPP (Large et al. 1994)
Tidal Mixing Scheme	St. Laurent et al. 2002	-
SSS Restoring	15 days to WOA13	6 days to WOA98
Northern/Southern Artifical Boundary	T & S restoring within 3° from the boundary	T & S restoring within 3° from the boundary
Important Narrow Channels	Straits of Gibraltar, Hormuz, and Bab el-Mandeb	-
Atmospheric Forcing	JRA55-do (3 hourly, 55km x 55km)	NCEP (daily, 2.5° x 2.5°)
River Runoff	CORE2 (monthly climatology)	-
Bulk Formula	Large & Yeager 2004	Rosati & Miyakoda 1988
Momentum Flux	Bulk formula using the relative wind speed	Momentum flux in NCEP (daily)
Hindcast Period	1958-2016	1950-2017
Initial Condition	T & S of OFES on Jan 1, 1958	OFES climatlogical run
Outputs	Daily mean every 3 days until 1989 Daily mean from 1990 Monthly mean	Snapshot every 3 days from 1980 Monthly Mean

Table 1: Descriptions of the quasi-global eddying hindcast simulations of OFES2 and OFES.

690

(a)

	OFES2	OFES	HadISST
RMS Amplitude of the Niño 3.4 index (℃)	0.95	0.93	0.89
Correlation with the Niño 3.4 in HadISST	0.963	0.880	-
RMS Amplitude of the DMI (℃)	0.52	0.38	0.32
Correlation with the DMI in HadISST	0.714	0.659	-

(b)

	OFES2	OFES	HadISST
RMS Amplitude of the Eastern Pole DMI(℃)	0.43	0.33	0.33
Correlation with the Eastern Pole DMI in HadISST	0.713	0.749	-
RMS Amplitude of the Western Pole DMI (℃)	0.31	0.41	0.33
Correlation with the Western Pole DMI in HadISST	0.847	0.751	-

Table 2: (a) RMS amplitude (°C) of the Niño3.4 index and the DMI for OFES2, OFES, and HadISST and their correlations between OFES2 and HadISST and between OFES and HadISST. (b) Same as (a) but the eastern and western pole DMIs.

695

	Improvements in OFES2 over OFES	New or remaining issues in OFES2
SST (3.1.1)	Suppressed cold biases in the equatorial and subtropical regions Suppressed warm biases in the high-latitude regions, the Arctic Ocean, the Sea of Okhotsk, and along the west coasts of South America and South Africa	Warm biases in the South Pacific and to the north of the Kuroshio Extension Warm and cold biases along the Gulf Stream
SSS (3.1.1)	Suppressed large biases by relatively weak SSS restoring	Salty biases in the North Atlantic and northern part of the Bay of Bengal and to the north of the South America
Mean SSH (3.1.2)	More realistic gyres in the subtropical North and South Pacific Suppressed too distinct propagations of the Agulhas Rings	Unrealistic pathways of the Gulf Stream and Kuroshio No Azores Current
SSH variability (3.1.2)	Suppressed too large variability along the strong currents	Slightly small in the regions away from the strong currents
Water property (3.2, 3.3, 3.4)	Suppressed biases in the subsurfaces of the Indonesian Seas, the Arabian Sea (salty outflows from the Persian Gulf and Red Sea), and the subtropical western Pacific	Lack of nonlocal tidal mixing in the Indonesian Seas Unrealistic subsurface in the northeastern subtropical Atlantic Ocean (salty outflow from the Mediterranean Sea)
El Niño and IOD (4)	Slightly higher correlations of the indexes with observations More realistic SST near the Sumatra and Java during the IOD events	

Table 3: Improvements in OFES2 over OFES and new or remaining issues in OFES2.